Geomorphology 317 (2018) 128–138

Contents lists available at ScienceDirect

Geomorphology

journal homepage: www.elsevier.com/locate/geomorph

Fluvial response to precipitation variations since 36 ka in the Hunshandake Sandy Land in North China

Cunjuan Lv [a], Xusheng Li [a,*], Zhiyong Han [a], Yong Wang [b], Yuwen Zhou [a], Mengyao Jiang [a], Qianqian Yang [a], Zhiwei Xu [a], Shuangwen Yi [a], Huayu Lu [a]

[a] School of Geography and Ocean Science, Nanjing University, Nanjing 210023, China
[b] Geological Institute, Chinese Academy of Geological Sciences, Beijing 100037, China

ARTICLE INFO

Article history:
Received 19 December 2017
Received in revised form 18 May 2018
Accepted 18 May 2018
Available online 24 May 2018

Keywords:
Fluvial terrace
East Asian monsoon
OSL dating
Hunshandake Sandy Land

ABSTRACT

The Hunshandake Sandy Land, which is highly sensitive to climate change, is located in North China along the margins of the area influenced by the East Asian monsoon. The upper reach of the Xilamulun River, which drains the Hunshandake Sandy Land, provides an opportunity to test the response of a river landform within a sandy region to climate change. We investigated terraces at 4 sites along a 38-km-long stretch and performed OSL dating on 26 terraces. The dating results revealed 23 terraces with unsaturated ages ranging from 0.3 ka to 36.2 ka. The observed relationship between the terrace heights and ages is abnormal, i.e., the terrace age does not increase with the terrace height. In this case, aeolian and fluvial interactions were analyzed, and a precipitation-dominated terrace formation model was developed. Higher terraces formed when the riverbed aggraded due to decreased sediment discharge and increased aeolian sand input during a period of reduced precipitation. In contrast, lower terraces developed when the riverbed eroded during a period of enhanced precipitation. We conclude that the terraces along this Hunshandake Sandy Land river respond to precipitation changes, even in the absence of background uplift.

1. Introduction

Fluvial terraces constitute an important component of the geomorphic system of a river. A terrace formation represents a geomorphic response to the quick, dynamic downcutting of a river. Tectonic movement and climate change are the two primary factors that can cause a river to downcut (Maddy et al., 2000; Merritts, 2007). Tectonic terraces form due to tectonic uplift, which enhances riverine downcutting. Climate change in relatively stable areas will dominate terrace development by altering the river discharge and sediment flux (Doğan, 2011). Consequently, climatic terraces may reveal glacial-interglacial cycles (Blum, 2013). Previous studies showed that fluvial terraces are capable of recording climate changes over a span from tens of thousands of years to millennia (Törnqvist, 2007). Aeolian and fluvial interactions constitute the usual geomorphic processes in arid environments (Bullard and McTainsh, 2003). Sediment-transporting rivers, which serve as interceptors for sand blowing downwind, may become the boundaries of deserts (Thomas et al., 1997). While deserts can supply sediments for rivers (Srivastava et al., 2005), fluvial sediments can also become the provenance of aeolian sands (Han et al., 2007). Aeolian sand deposition could induce the bifurcation of a river (Tooth, 1999) or lead to the formation of dammed lakes and swamps (Loope et al., 1995; Mason et al., 2004).

The Hunshandake Sandy Land, which is a vulnerable ecological environment that is highly sensitive to climate change (Zhou et al., 2008), is situated along the marginal area of the East Asian monsoon (EAM). Extensive research has been conducted on environmental changes throughout the Hunshandake Sandy Land, including the history of aeolian activity since the Last Glacial Maximum (Lu et al., 1999, 2005; Jin et al., 2003; Zhou et al., 2005, 2013) and the changes in the vegetation and lake level during the Holocene (Xiao et al., 2008, 2009; Liu et al., 2016; Goldsmith et al., 2017). The upper reach of the Xilamulun River drains the Hunshandake Sandy Land. One study suggested that the aridification that occurred at 4.2 ka resulted from the capture of underground water by the Xilamulun River (Yang et al., 2015). However, this hypothesis lacks supporting evidence from fluvial landforms. Moreover, the response of the Xilamulun River to climate change remains unknown.

Consequently, we surveyed the fluvial terraces in the upper reach of the Xilamulun River. The terrace heights were acquired from 1:25,000 digital elevation model (DEM) data. The terrace ages were determined through the optically stimulated luminescence (OSL) dating of fluvial sediments. The reconstructed temporal sequence of these terrace heights could represent the response of the river landform to climate change.

* Corresponding author.
E-mail address: lixusheng@nju.edu.cn (X. Li).

https://doi.org/10.1016/j.geomorph.2018.05.016
0169-555X/

2. Regional setting

The Hunshandake Sandy Land is situated in the middle of the Inner Mongolia Autonomous Region and is approximately 250 km to the north of Beijing (Fig. 1b). The Hunshandake Sandy Land covers an area of 30,000 km^2 and spans a distance of 400 km from east to west and 80 km from south to north. The mean elevation of the Hunshandake Sandy Land is 1100 m; it exhibits a gentle topography, and the ground elevation slowly declines from the southeast to the northwest. Most of the dunes in the Hunshandake Sandy Land are either fixed or semi-fixed. Numerous lakes exist throughout the Sandy Land with few observable rivers.

The Hunshandake Sandy Land is located in a temperate zone with a semi-arid monsoon climate, and it is characterized by low temperatures and strong winds (Zhou et al., 2013). The annual mean temperature is 1.6 °C, the annual mean precipitation is 386 mm, and the annual mean evaporation is 1761 mm. To estimate the effects of the wind regime on sand drift, we collected one measure of wind data every 3 h from Apr. 2016 to Mar. 2017 at the meteorological station in Xilinhaote, which is located approximately 37 km to the north of the Hunshandake Sandy Land. A sand rose was calculated by assuming a threshold wind velocity of 6 m/s (Fig. 1c). The drift potential (DP) is 75 VU (vector units), the resultant drift potential (RDP) is 23 VU, and the resultant drift direction (RDD) is 99°; these values are generally consistent with those indicated by the parabolic dunes in the Hunshandake Sandy Land. The sand rose also illustrates that the Hunshandake Sandy Land exhibits a broad unimodal wind regime and is characterized by a low-energy wind environment.

The Xilamulun River, which constitutes the upper reach of the Liaohe River, is 397 km long with a relief of 1515 m. The drainage area is 32,629 km^2, and the annual mean runoff is 7.31×10^8 m^3. Two tributaries drain the Hunshandake Sandy Land: the Huangyuan River and the Saling River. The former originates from the interior of the Hunshandake Sandy Land, and the latter is sourced from the Yan Mountains (Fig. 1a). The drainage basin of the Xilamulun River is relatively

Table 1
Characteristics of the fluvial terraces of the Xilamulun River.

Site	Riverbed elevation (m)	Location	Terrace number	Length (m)	Width (m)	Height (m)
Tianshuyingzi (TSYZ)	1170	Left bank	$T_{tsyz-L-1173}$	100	20	3
			$T_{tsyz-L-1175}$	100	50	5
		Right bank	$T_{tsyz-R-1179}$	100	30	9
Xiangshuishuiku (XSSK)	1116	Left bank	$T_{xssk-L-1116}$	200	100	2
			$T_{xssk-L-1122}$	500	50	6
			$T_{xssk-L-1127}$	500	80	11
			$T_{xssk-L-1140}$	900	100	24
		Right bank	$T_{xssk-R-1126}$	500	50	10
			$T_{xssk-R-1145}$	600	120	29
			$T_{xssk-R-1217}$	1000	100	101
			$T_{xssk-R-1225}$	1200	80	109
Shimenshuiku (SMSK)	1080	Right bank	$T_{smsk-R-1085}$	200	30	5
			$T_{smsk-R-1105}$	300	50	35
			$T_{smsk-R-1154}$	300	50	74
			$T_{smsk-R-1173}$	100	50	93
			$T_{smsk-R-1193}$	1000	500	113
			$T_{smsk-R-1219}$	300	50	139
Henanyingzi (HNYZ)	1020	Left bank	$T_{hnyz-L-1024}$	500	300	4
			$T_{hnyz-L-1034}$	500	50	14
			$T_{hnyz-L-1040}$	200	150	20
			$T_{hnyz-L-1061}$	1000	100	41
			$T_{hnyz-L-1061}^{*}$	1000	100	41
			$T_{hnyz-L-1119}$	600	300	99
		Right bank	$T_{hnyz-R-1023}$	500	100	3
			$T_{hnyz-R-1031}$	1000	100	11
			$T_{hnyz-R-1053}$	1000	100	33
			$T_{hnyz-R-1127}$	2000	50	107

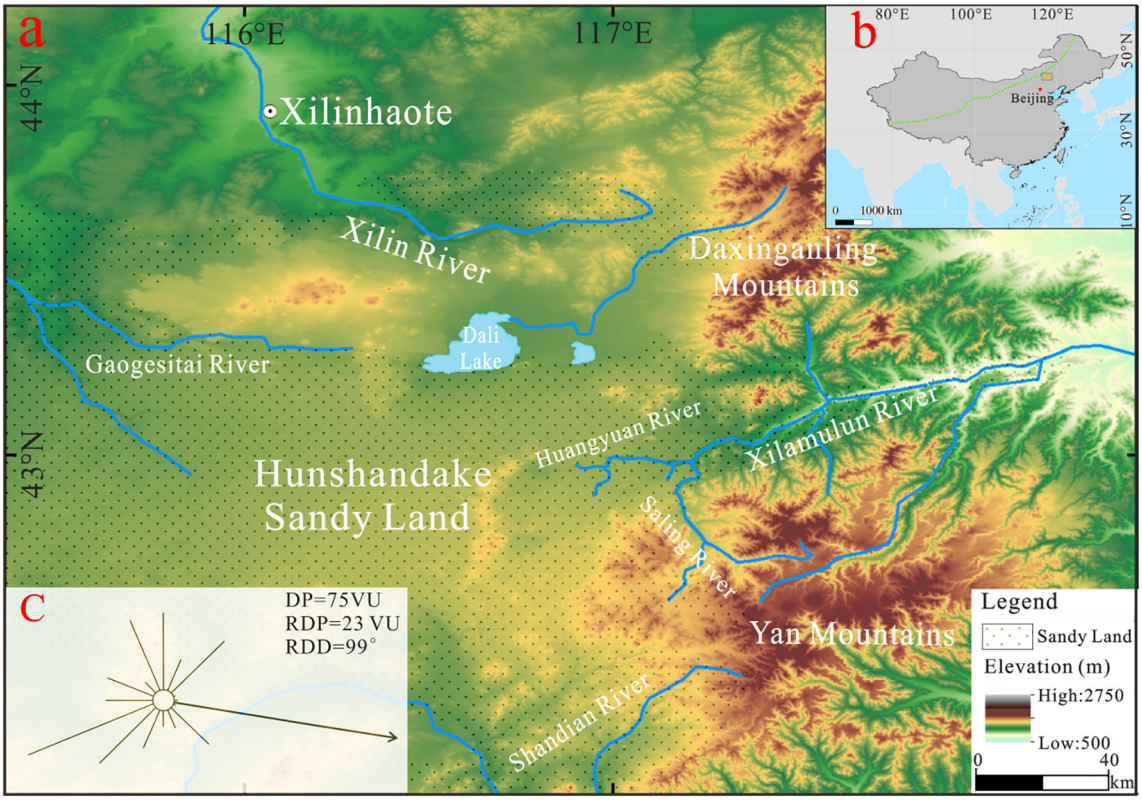

Fig. 1. Geographical setting of the Xilamulun River. (a) DEM image showing the rivers draining the Hunshandake Sandy Land; (b) Inset map showing the front of the East Asian monsoon represented by the green line (Chen et al., 2015); (c) Sand rose. The DP (drift potential, in vector units or VU) is a measure of the relative sand-moving capability of wind in a given direction, while the RDD (resultant drift direction, in vector units) is the net trend of the sand drift. The wind data employed are one measure per 3 h from Apr. 2016 to Mar. 2017 at the meteorological station in Xilinhaote.

wide in the upper reach. Additional tributaries originate from the southern bank. The Xilamulun River flows toward the east as a sandy braided river, while the river valley within the Hunshandake Sandy Land is narrow and deep, which suggests that the river has experienced intensive downcutting.

3. Material and methods

3.1. Terrace characteristics and sample collection

The fluvial terraces of the Xilamulun River can be easily identified in the field according to their step-like shape and alluvial deposits. Both fill terraces and erosion terraces were discovered; they were distributed at different heights ranging from meters to more than one hundred meters in the upper reach of the Xilamulun River (Table 1). We conducted investigations at 4 sites (Fig. 2a), namely, Tianshuyingzi (TSYZ), Xiangshuishuiku (XSSK), Shimenshuiku (SMSK) and Henanyingzi (HNYZ), where these terraces are readily detectable on satellite imagery. We collected a DEM at a mapping scale of 1:25,000 with a mean accuracy of ±2 m. The longitude and latitude coordinates of the terraces were measured using a GPS receiver. The elevation was determined using the DEM, and the location was further verified utilizing Google Earth.

The river valley at TSYZ is narrow (Fig. 2b). Three terraces, one on the right bank ($T_{tsyz\text{-}R\text{-}1179}$) and two on the left bank ($T_{tsyz\text{-}L\text{-}1173}$,

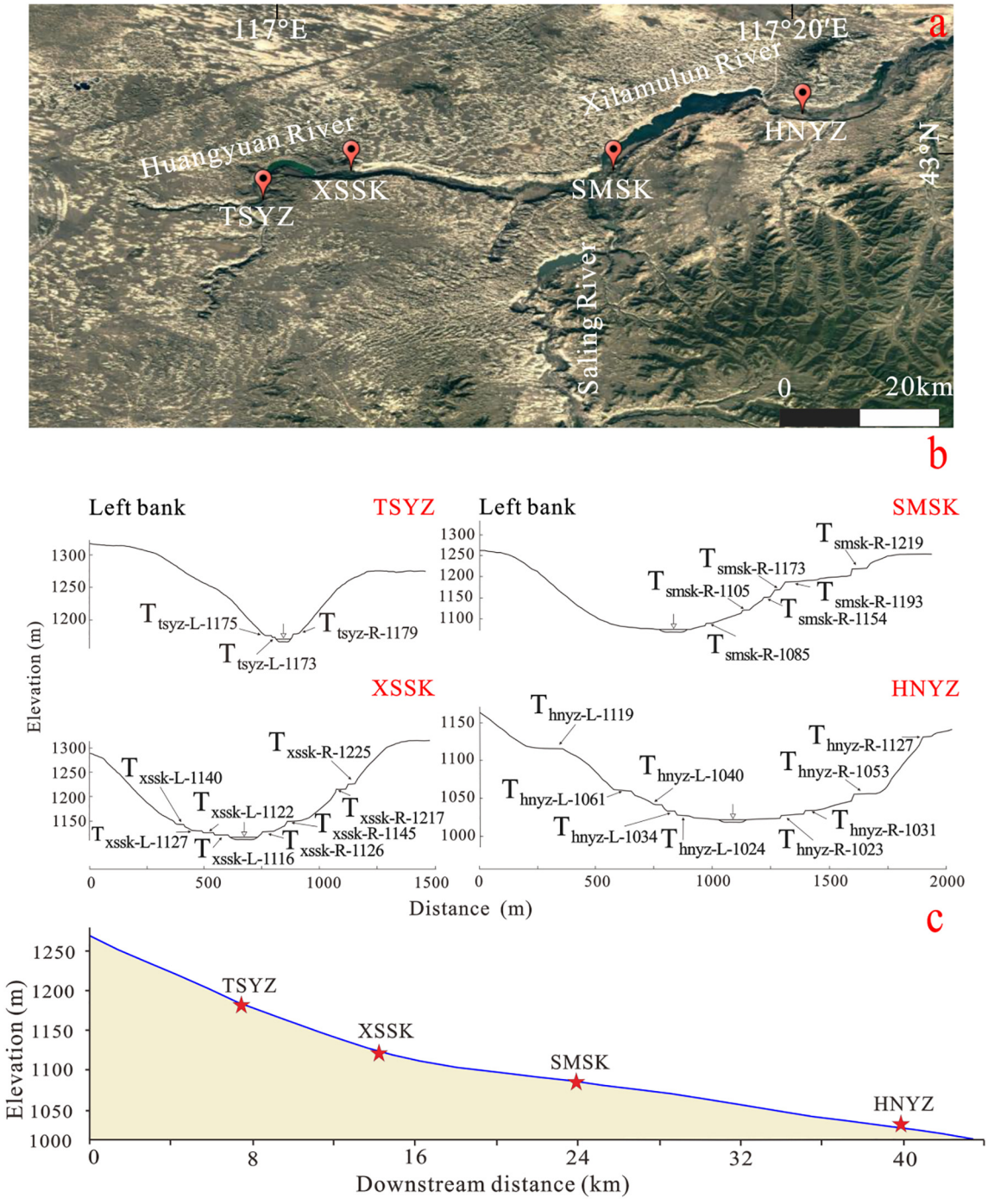

Fig. 2. Morphology of the Xilamulun River. (a) Satellite images of the Xilamulun River within the Hunshandake Sandy Land (from Google Earth); (b) Transverse profiles at Tianshuyingzi (TSYZ), Xiangshuishuiku (XSSK), Shimenshuiku (SMSK) and Henanyingzi (HNYZ) exhibiting a downstream widening of the river valley; (c) Longitudinal profile of the Xilamulun River.

$T_{tsyz\text{-}L\text{-}1175}$), developed on the slope of the valley (Fig. 3). The fluvial sediments are composed of fine and medium sands that occasionally contain mollusk fragments. Generally, the fluvial sediments can be divided into two horizons: an upper sandy soil and a lower sand, the bottom of which is unseen. The river valley becomes wider and more symmetric at XSSK (Fig. 2b). The right and left bank both exhibit four terraces (Fig. 4). The fluvial sediments of two terraces ($T_{xssk\text{-}L\text{-}1122}$ and $T_{xssk\text{-}R\text{-}1217}$) are composed of fine and medium sands that occasionally contain granules, while the other terraces do not yield granules. The river valley is less symmetric at SMSK, and there is no terrace on the cutbank (left bank). The six terraces on the right bank share a similar stratigraphic sequence (Fig. 5). The fluvial sediments therein can be divided into three horizons: the upper horizon, which is composed of gravelly sandy soil, the middle horizon that comprises sandy gravel, and the lower horizon composed of gravelly sand (the bottom of which is unseen). The upper and middle horizons have a thickness of tens of centimeters. Most gravels are sub-angular or sub-rounded with clast diameters that range from 2 cm to 10 cm (up to 30 cm). Aeolian sand deposits with a thickness of 190 m are well exposed on the cutbank. Three OSL samples (Shimen-58 m, Shimen-134 m, and Shimen-162 m) were collected from the aeolian sediments. At HNYZ, where the valley is the widest, we discovered five terraces on the left bank and four terraces on the right bank (Fig. 2b). All of the terraces here have a stratigraphic sequence similar to that at SMSK. Among them, two terraces ($T_{hnyz\text{-}R\text{-}1031}$, $T_{hnyz\text{-}R\text{-}1127}$) have suffered gully erosion, and thus, trough cross-bedding is observed along the lower horizon (Fig. 6).

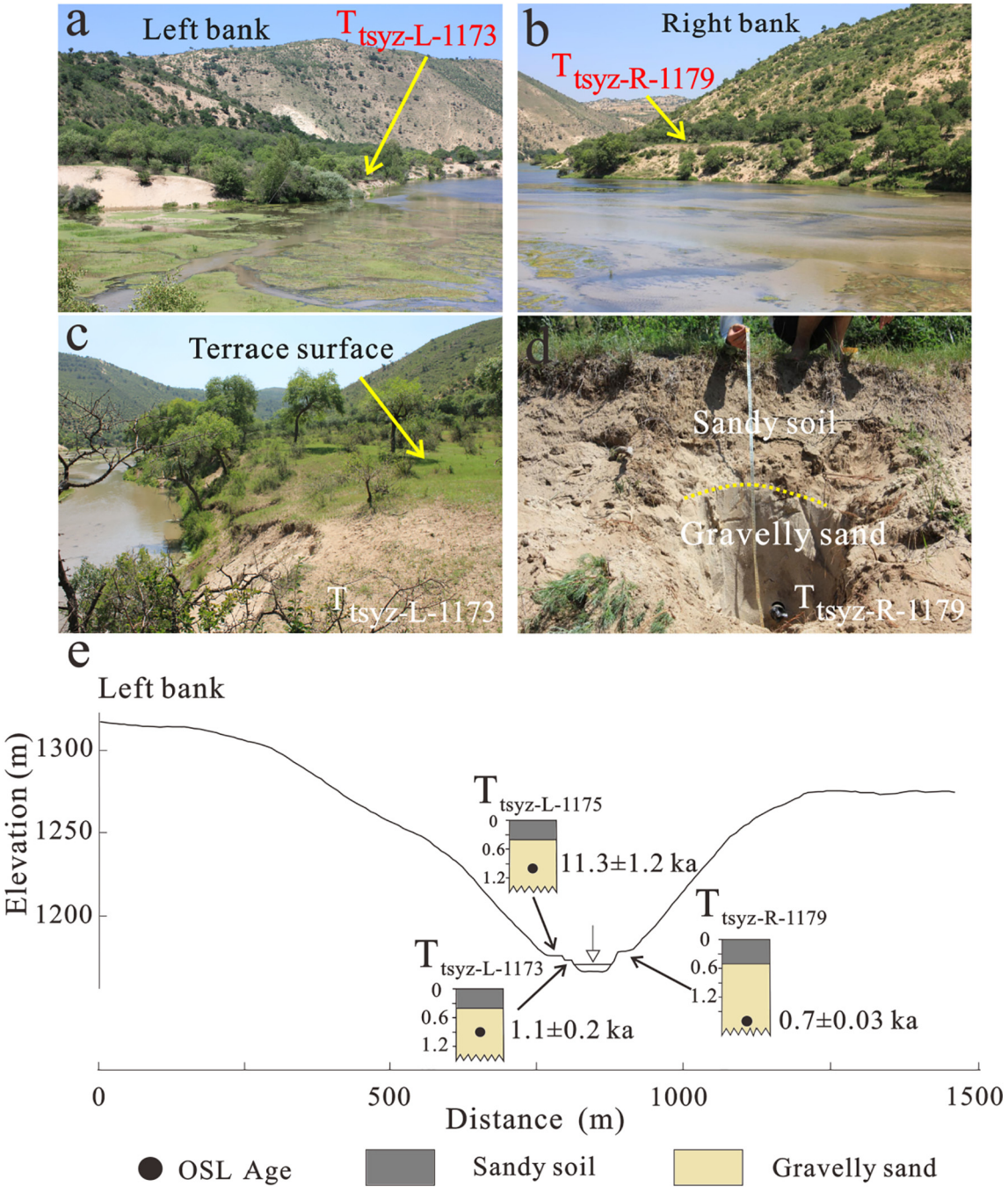

Fig. 3. Fluvial terraces at Tianshuyingzi (TSYZ). (a) The terraces on the left bank; (b) The terraces on the right bank; (c) Surface of terrace $T_{tsyz\text{-}L\text{-}1173}$; (d) Stratigraphic sequence composed of sandy soil and gravelly sand within terrace $T_{tsyz\text{-}R\text{-}1179}$; (e) Sampling locations and OSL ages. The numbers to the left of the stratigraphic columns represent the depth in meters.

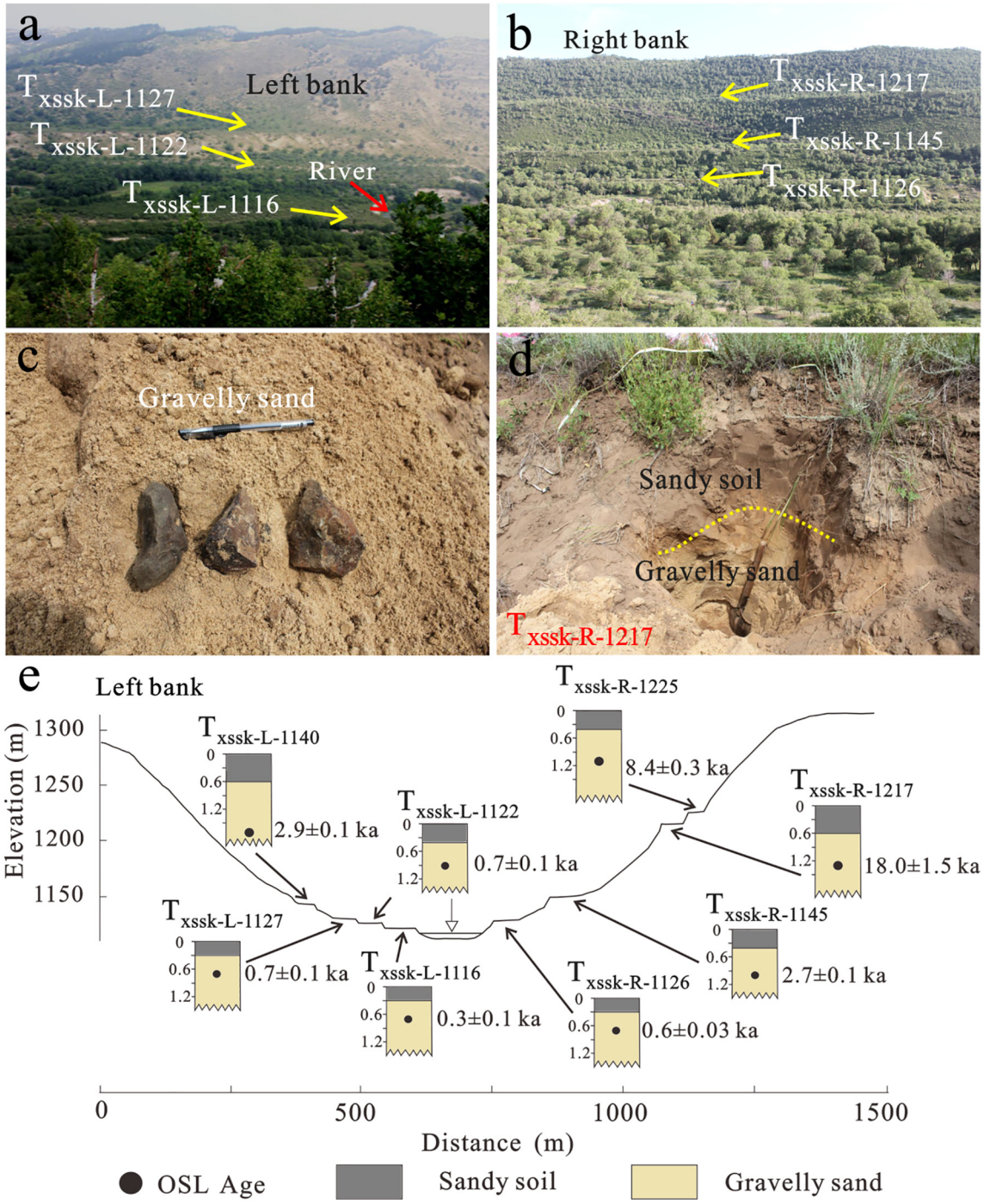

Fig. 4. Fluvial terraces at Xiangshuishuiku (XSSK). (a) The terraces on the left bank; (b) The terraces on the right bank; (c) Gravel-sized clasts within the gravelly sand; (d) Stratigraphic sequences composed of sandy soil and gravelly sand within terrace $T_{xssk-R-1217}$; (e) Sampling locations and OSL ages. The numbers to the left of the stratigraphic columns represent the depth in meters.

The fluvial terraces have different widths and lengths; their widths range from 50 m to 500 m, and their lengths range from 50 m to 1000 m (Table 1). The terrace surfaces, which gently dip downstream and toward the riverbed, are usually flat except for the occasional appearance of small blowouts. The terraces exhibit two types of stratigraphic sequences: a two-horizon sequence and a three-horizon sequence. The former is composed of an upper horizon (sandy soil) and a lower horizon (sand or gravelly sand) (Figs. 3 and 4), while the latter has an extra middle horizon (sandy gravel) (Figs. 5 and 6). The lower horizon occasionally contains mollusk fragments or granules (Fig. 3d) and exhibits developed trough cross-bedding (Fig. 6d). These features indicate that the fluvial sediments were deposited in a riverbed environment. The upper horizon shows signs that it has suffered post-depositional wind reworking, and the middle horizon is less homogenous. As a result, all of the OSL samples were collected from the homogenous lower horizon.

A 20-cm-long stainless steel tube was used to acquire the OSL samples. The surface layer with a thickness of at least 30 cm was removed before hammering the tube into the sediments. The sediment-filled tube was then dug out from the ground and sealed with tape. We

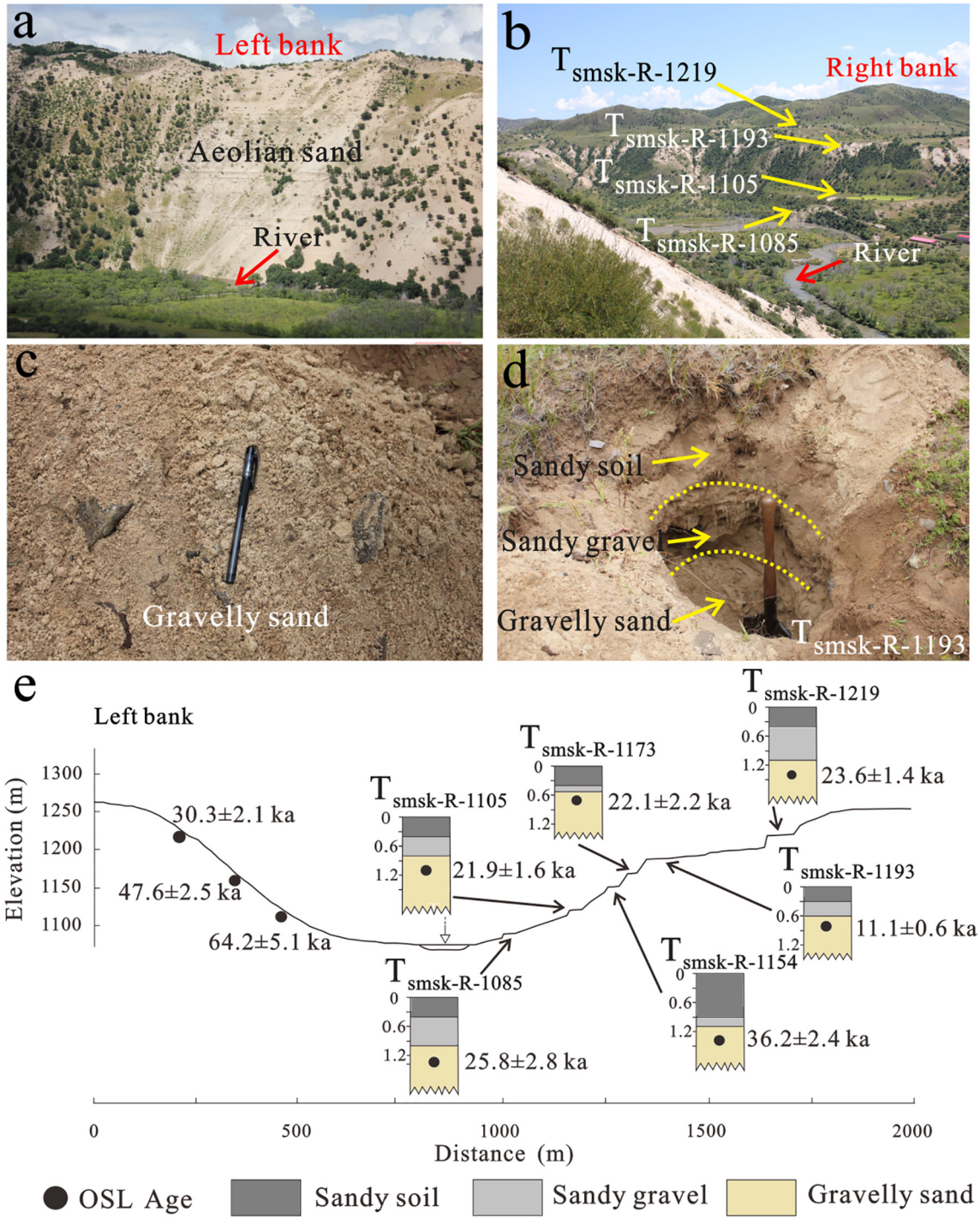

Fig. 5. Fluvial terraces at Shimenshuiku (SMSK). (a) Strata composed of aeolian sands on the left bank (cutbank); (b) The terraces on the right bank; (c) Gravel-sized clasts within the gravelly sand; (d) Stratigraphic sequence composed of sandy soil, sandy gravel and gravelly sand within terrace $T_{smsk\text{-}R\text{-}1193}$; (e) Sampling locations and OSL ages. The numbers to the left of the stratigraphic columns represent the depth in meters. The three OSL ages on the left bank reveal that the aeolian sands are older than the fluvial sediments.

collected 27 OSL samples from 26 terraces; one sample is a parallel sample taken from HNYZ ($T_{hnyz\text{-}L\text{-}1061}$*).

3.2. OSL dating

Sediments collected near the end of the tube were used for analyses of the water content and the U, Th and K contents. The elemental contents were measured at the China Institute of Atomic Energy using the neutron activation method. A pretreatment procedure (Zhang et al., 2008) was applied to extract coarse-grained quartz (90–125 μm). The quartz purity was checked using the IR-test. The single-aliquot regenerative-dose (SAR) protocol (Murray and Wintle, 2000; Wintle and Murray, 2006) and an exponential fit (Fig. 7a, b) were adopted to measure the equivalent dose (D_e). The D_e value of each sample is the average of each disc, and the error is the standard error of 16 discs. The value of D_e was measured on a Risø TL/OSL-DA-20 reader. The OSL ages were calculated using the program DR calculator (Tsakalos et al., 2015).

To evaluate the effectiveness of the SAR protocol, dose recovery experiments and preheat plateau tests were performed on two

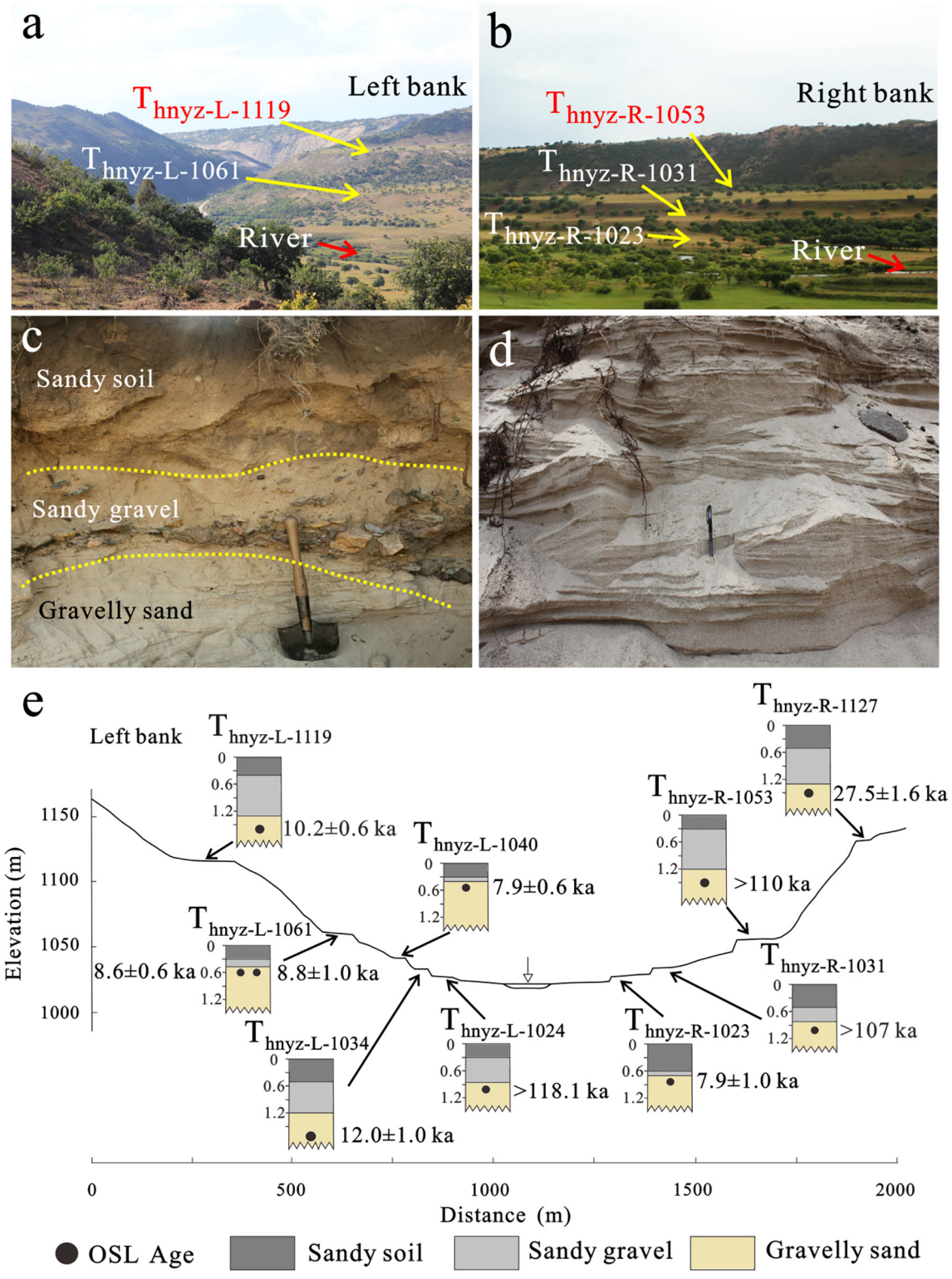

Fig. 6. Fluvial terraces at Henanyingzi (HNYZ). (a) The terraces on the left bank; (b) The terraces on the right bank; (c) Stratigraphic sequence composed of sandy soil, sandy gravel and gravelly sand within terrace $T_{hnyz\text{-}R\text{-}1127}$; (d) Trough cross-bedding in a gravelly sand; (e) Sampling locations and OSL ages. The numbers to the left of the stratigraphic columns represent the depth in meters.

selected samples ($T_{smsk\text{-}R\text{-}1154}$ and $T_{hnyz\text{-}L\text{-}1061}$*). Based on the test results (Fig. 7c), a 240 °C preheat temperature and a 180 °C cut heat temperature were chosen for the D_e measurements. The relative difference between the recovered doses and the given doses of both samples was smaller than 0.5%. All of the measured discs yielded a mean recycling ratio of unity (Fig. 7d).

4. Results

4.1. OSL ages

Among the 26 terraces, 3 terraces ($T_{hnyz\text{-}L\text{-}1024}$, $T_{hnyz\text{-}R\text{-}1031}$, and $T_{hnyz\text{-}R\text{-}1053}$) are excluded from further analysis since they yielded

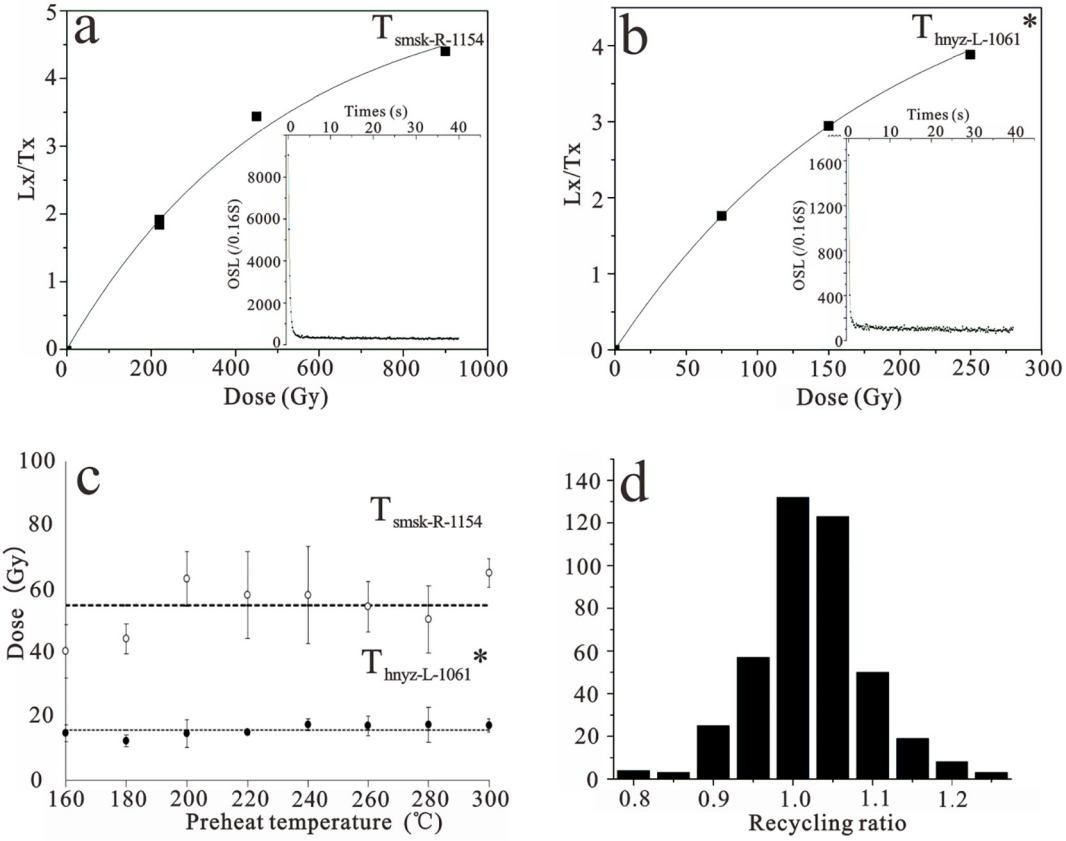

Fig. 7. Luminescence characteristics for coarse-grained quartz (90–125 μm). (a) and (b) Dose response curves for aliquots of samples $T_{smsk\text{-}R\text{-}1154}$ and $T_{hnyz\text{-}L\text{-}1061}$*, respectively (inset shows the natural decay curves measured at 125 °C and at 90% blue LED power); (c) Preheat plateau tests of the samples $T_{smsk\text{-}R\text{-}1154}$ and $T_{hnyz\text{-}L\text{-}1061}$*. Three aliquots were measured at each temperature, and the error bars represent 1 standard error. The dash-dot line is drawn at the average D_e value over the interval of 180–280 °C; (d) Histogram of the recycling ratios for all samples (measured as part of the D_e determination).

saturated OSL ages (Table 2). The OSL ages of the parallel samples, namely, $T_{hnyz\text{-}L\text{-}1061}$ and $T_{hnyz\text{-}L\text{-}1061}$*, are 8.8 ± 1.0 ka and 8.6 ± 0.6 ka, respectively. They are equivalent within the margin of error, thereby testifying that the OSL ages are reliable. The mean water contents of the measured samples reach as low as 1.33%, but the average saturated water content is 19%. The OSL ages increase by ~20% if the saturated water content is used for the age calculation. The actual water content of a sample is mainly dependent on its burial history, i.e., the length of time it has been situated below the water table. In this study, the OSL ages calculated using the measured and saturated water contents should be treated as the lower and upper limits of the burial age, respectively. For the purpose of simplifying the terrace correlation, only ages calculated using the measured water contents are analyzed in the following discussion.

4.2. Variability in terrace height

Disregarding the saturated OSL ages, the age of the oldest terrace is 36.2 ka, and the age of the youngest terrace is 0.3 ka. Contrary to a normal stream, some of the terraces among the four sites along the Xilamulun River are out of sequence, i.e., the terrace ages do not increase with the height (Figs. 3, 4, 5 and 6), even when considering an ~20% age underestimation due to uncertainties in the water content. We can accordingly construct the temporal sequence of the terrace height for the Xilamulun River (Fig. 8). Because a terrace represents an ancient riverbed, we can see that the height of the ancient riverbed of the Xilamulun River has changed greatly since 36.2 ka. The ancient riverbed was relatively high at 36.2 ka, 27.5 ka, 23.6 ka, 18.0 ka, 11.1 ka, 8.4 ka and 2.7 ka; meanwhile, it was relatively low at 25.8 ka, 21.9 ka, 11.3 ka, 8.8 ka, 7.9 ka and 1.1 ka (Fig. 8). The variability in the riverbed height is the largest between 11.3 ka and 7.9 ka. A large variability is also observed for another period from 27.5 ka to 21.9 ka.

5. Discussion

5.1. Out-of-sequence terraces

The age of a fluvial terrace usually increases with its height (Penkman et al., 2011). Our results show that the terrace ages are independent of their height in the upper reach of the Xilamulun River (Fig. 8). Since both the age differences and the height differences among the terraces significantly exceed the measurement error, we assert that the observed out-of-sequence terraces are credible. This seems to be a prevailing phenomenon, because we found these out-of-sequence terraces at all of the studied sites. We can almost exclude the possibility of mistaking aeolian sediments for fluvial sediments, because the aeolian sands in the Hunshandake Sandy Land were deposited during an earlier stage lasting from 64 ka to 30 ka (Fig. 5); thus, these sands are obviously older than the fluvial sediments. The Xilamulun River, which has a wide and shallow channel, constitutes a sandy braided river with a low suspended load. This hydrologic condition favors sunlight bleaching, and consequently, the ages of the alluvial sediments are almost unaffected by residual OSL signals during deposition. In addition, the measured sediments are lithologically homogenous, and the contents of radioactive elements showed minor variations (Table 2). The probability of overestimating or underestimating an OSL age due to an abnormal element content is very low. Thus, the out-of-sequence terrace ages are not the product of inaccurate OSL dating.

Table 2
OSL dating results for the Xilamulun River.

Sample	Latitude (°)	Longitude (°)	Elevation (m)	Depth (m)	Water content (%)	U (ppm)	Th (ppm)	K (%)	Dose rate (Gy/ka)	Equivalent dose (Gy)	Age[1] (ka)	Age[2] (ka)
$T_{tsyz\text{-}L\text{-}1173}$	42.97	116.99	1173	0.9	1.7	0.52 ± 0.04	1.51 ± 0.08	1.19 ± 5.08	1.61 ± 0.04	1.72 ± 0.31	1.1 ± 0.2	1.3 ± 0.2
$T_{tsyz\text{-}L\text{-}1175}$	42.97	116.99	1175	1.7	0.9	0.45 ± 0.04	1.69 ± 0.08	1.39 ± 4.6	1.71 ± 0.04	19.2 ± 1.9	11.3 ± 1.2	13.7 ± 1.7
$T_{tsyz\text{-}R\text{-}1179}$	42.97	116.99	1179	1	1.2	0.58 ± 0.05	1.95 ± 0.08	1.43 ± 4.18	1.90 ± 0.05	1.34 ± 0.04	0.7 ± 0.03	0.8 ± 0.1
$T_{xssk\text{-}L\text{-}1116}$	42.99	117.05	1116	0.9	1.0	0.43 ± 0.04	1.54 ± 0.08	1.37 ± 5.08	1.78 ± 0.05	0.55 ± 0.08	0.3 ± 0.1	0.3 ± 0.1
$T_{xssk\text{-}L\text{-}1122}$	42.99	117.05	1122	1	1.5	0.69 ± 0.06	2.28 ± 0.09	1.03 ± 4.09	1.54 ± 0.04	1.13 ± 0.10	0.7 ± 0.1	0.9 ± 0.1
$T_{xssk\text{-}L\text{-}1127}$	42.99	117.05	1127	0.65	1.9	0.57 ± 0.05	1.65 ± 0.08	1.08 ± 4.68	1.49 ± 0.04	1.03 ± 0.06	0.7 ± 0.1	0.8 ± 0.1
$T_{xssk\text{-}L\text{-}1140}$	42.99	117.04	1225	2.6	1.5	0.38 ± 0.04	1.29 ± 0.07	1.89 ± 5.5	2.12 ± 0.05	6.20 ± 0.18	2.9 ± 0.1	3.5 ± 0.3
$T_{xssk\text{-}R\text{-}1126}$	42.99	117.05	1126	0.7	1.2	0.43 ± 0.04	1.68 ± 0.08	1.24 ± 4.68	1.62 ± 0.05	1.03 ± 0.04	0.6 ± 0.03	0.7 ± 0.1
$T_{xssk\text{-}R\text{-}1145}$	42.99	117.05	1145	1	0.4	0.44 ± 0.01	1.55 ± 0.08	2.41 ± 5.08	2.84 ± 0.06	7.75 ± 0.17	2.7 ± 0.1	3.4 ± 0.3
$T_{xssk\text{-}R\text{-}1217}$	42.99	117.04	1217	1.3	1.0	0.42 ± 0.04	1.88 ± 0.08	2.06 ± 4.38	2.48 ± 0.05	44.7 ± 3.6	18.0 ± 1.5	21.8 ± 2.3
$T_{xssk\text{-}R\text{-}1225}$	42.99	117.04	1225	1.1	2.5	0.44 ± 0.04	1.51 ± 0.08	1.91 ± 5.08	2.28 ± 0.06	19.2 ± 0.6	8.4 ± 0.3	10.0 ± 0.8
$T_{smsk\text{-}R\text{-}1085}$	42.99	117.23	1085	1.3	0.4	0.33 ± 0.03	1.3 ± 0.08	1.72 ± 5.80	2.03 ± 0.11	52.3 ± 5.0	25.8 ± 2.8	31.5 ± 3.8
$T_{smsk\text{-}R\text{-}1105}$	42.99	117.23	1105	1.1	1.3	0.38 ± 0.04	1.62 ± 0.09	2.22 ± 5.69	2.61 ± 0.13	57.1 ± 3.1	21.9 ± 1.6	26.5 ± 2.4
$T_{smsk\text{-}R\text{-}1154}$	42.98	117.22	1154	1.3	1.0	0.49 ± 0.04	2.1 ± 0.10	1.24 ± 4.64	1.65 ± 0.08	59.6 ± 2.5	36.2 ± 2.4	43.9 ± 3.7
$T_{smsk\text{-}R\text{-}1173}$	42.98	117.22	1173	0.7	2.9	0.36 ± 0.04	1.92 ± 0.10	1.43 ± 5.00	1.77 ± 0.09	39.1 ± 3.4	22.1 ± 2.2	26.2 ± 3.0
$T_{smsk\text{-}R\text{-}1193}$	42.98	117.23	1193	0.8	0.8	0.34 ± 0.03	1.46 ± 0.08	1.55 ± 5.68	1.89 ± 0.10	20.9 ± 0.6	11.1 ± 0.6	13.4 ± 1.0
$T_{smsk\text{-}R\text{-}1219}$	42.98	117.23	1219	1.4	0.8	0.35 ± 0.03	1.62 ± 0.09	1.55 ± 5.69	1.94 ± 0.10	45.7 ± 1.5	23.6 ± 1.4	28.6 ± 2.3
$T_{hnyz\text{-}L\text{-}1024}$	43.03	117.36	1024	1	1.1	0.39 ± 0.04	1.49 ± 0.07	1.51 ± 5.07	1.90 ± 0.05	>225	>118	>143
$T_{hnyz\text{-}L\text{-}1034}$	43.03	117.36	1034	1.7	0.4	0.62 ± 0.05	1.71 ± 0.08	0.95 ± 4.58	1.36 ± 0.04	16.4 ± 1.3	12.0 ± 1.0	14.7 ± 1.5
$T_{hnyz\text{-}L\text{-}1040}$	43.04	117.35	1040	0.5	2.8	0.37 ± 0.04	1.33 ± 0.08	1.75 ± 5.88	2.15 ± 0.11	17.0 ± 0.9	7.9 ± 0.6	9.4 ± 0.8
$T_{hnyz\text{-}L\text{-}1061}$	43.04	117.35	1061	0.6	0.7	0.54 ± 0.04	2.18 ± 0.1	1.26 ± 4.64	1.83 ± 0.09	16.1 ± 1.7	8.8 ± 1.0	10.7 ± 1.4
$T_{hnyz\text{-}L\text{-}1061}^{*}$	43.04	117.34	1062	0.8	1.9	0.64 ± 0.05	1.42 ± 0.07	1.43 ± 5.27	1.81 ± 0.0.5	15.5 ± 0.9	8.6 ± 0.6*	10.3 ± 1.0*
$T_{hnyz\text{-}L\text{-}1119}$	43.04	117.34	1119	1.6	2.8	1.08 ± 0.06	1.88 ± 0.08	1.41 ± 4.38	1.94 ± 0.0.5	19.7 ± 1.1	10.2 ± 0.6	12.1 ± 1.1
$T_{hnyz\text{-}R\text{-}1023}$	43.03	117.36	1023	0.8	0.8	0.45 ± 0.04	1.75 ± 0.09	1.62 ± 5.49	1.96 ± 0.10	15.8 ± 1.9	7.9 ± 1.0	9.6 ± 1.3
$T_{hnyz\text{-}R\text{-}1031}$	43.03	117.36	1031	1	1.0	0.35 ± 0.04	1.54 ± 0.09	1.61 ± 5.69	1.10 ± 0.10	>214	>107	>130
$T_{hnyz\text{-}R\text{-}1053}$	43.03	117.36	1053	1.5	1.7	0.32 ± 0.03	1.42 ± 0.08	1.73 ± 5.68	2.06 ± 0.10	>228	>110	>133
$T_{hnyz\text{-}R\text{-}1127}$	43.04	117.33	1127	1.5	0.6	0.42 ± 0.03	1.4 ± 0.08	1.36 ± 5.63	1.70 ± 0.09	46.6 ± 1.3	27.5 ± 1.6	33.5 ± 2.6
Shimen-58 m	42.99	117.21	1212	58	2.53	0.45 ± 0.04	1.79 ± 0.10	1.92 ± 0.06	2.0 ± 0.06	61.7 ± 3.8	30.3 ± 2.1	36.1 ± 3.5
Shimen-134 m	42.99	117.21	1136	134	0.94	0.55 ± 0.04	2.11 ± 0.11	2.50 ± 0.07	2.76 ± 0.06	131.6 ± 6.4	47.6 ± 2.5	57.8 ± 0.1
Shimen-162 m	42.99	117.21	1108	162	2.08	0.37 ± 0.03	1.56 ± 0.10	2.17 ± 0.06	2.32 ± 0.05	149.3 ± 11.3	64.2 ± 5.1	76.9 ± 7.8

Note: the age with an asterisk is given using the parallel sample. The age data in columns Age[1] and Age[2] are calculated using the measured and saturated water contents.

5.2. Model of terrace formation

Fluvial terraces can reflect tectonic movements, climate change and fluctuations in the base level of erosion. The valley shoulders in the upper reach of the Xilamulun River gradually decrease in height downstream. The valley shoulders on both banks are at nearly the same elevation, indicating the absence of fault offset along the river. In addition, the longitudinal profile (Fig. 2c) does not exhibit any knickpoint induced by fault movement or headward erosion. Therefore, we can consider the terraces of the Xilamulun River as climatic terraces.

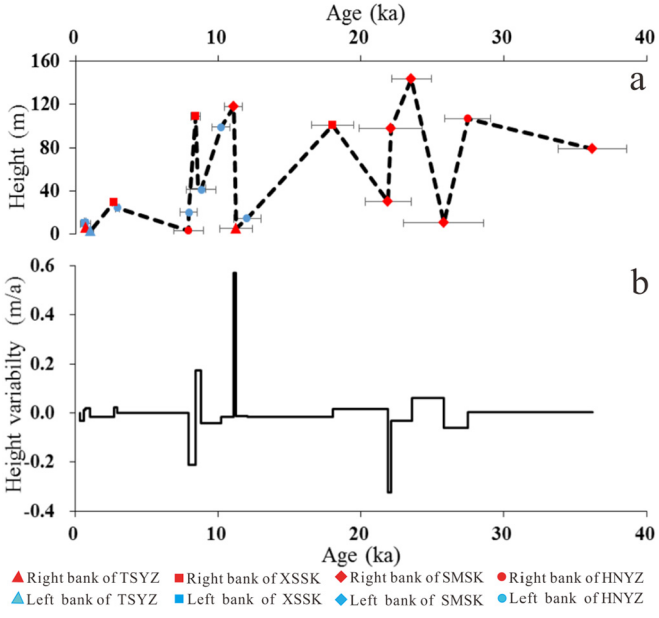

Fig. 8. Temporal sequence of each fluvial terrace height. (a) Height of each fluvial terrace; (b) Variability in the terrace height.

Out-of-sequence terraces indicate that the formation of a lower-elevation terrace preceded that of a higher-elevation terrace. Lower terraces will become buried when a river changes from downcutting to aggradation. A fill terrace may form when the river renews downcutting after the deposition of the higher terrace. When a river downcuts low enough, the buried terrace will be exposed (Fig. 9). It is therefore clear that this model is different from that in which background uplift is necessary for cyclic changes in the climate that drive terrace formation (Bridgland and Westaway, 2008). Buried terraces can survive because they are generally covered by a layer of sandy gravel, which prevents the terrace from being eroded. Plants and roots on lower terraces that are absent this sandy gravel layer prior to burial may have a similar effect.

5.3. Precipitation-driven fluvial process

The state of erosion and deposition of the riverbed of the Xilamulun River is related to two factors: downstream sediment discharge and aeolian sand input. When the sediment discharge is lower than the aeolian sand input, the riverbed will aggrade and rise; on the contrary, when opposite is true, the riverbed will erode and depress. As data regarding the bedload discharge of the Xilamulun River are not available, we cannot determine the exact relationship between the bedload discharge and runoff. Some studies found a power function relationship that exists between the bedload discharge and runoff, i.e., larger runoff rates correlate with a larger bedload discharge (Faye et al., 1978; Clark and Woods, 2000).

The factors that can influence runoff have been investigated (Irwin et al., 2005; DiBiase and Whipple, 2011; Gulick, 2001). The primary influencing factors are believed to be precipitation and melt water. No

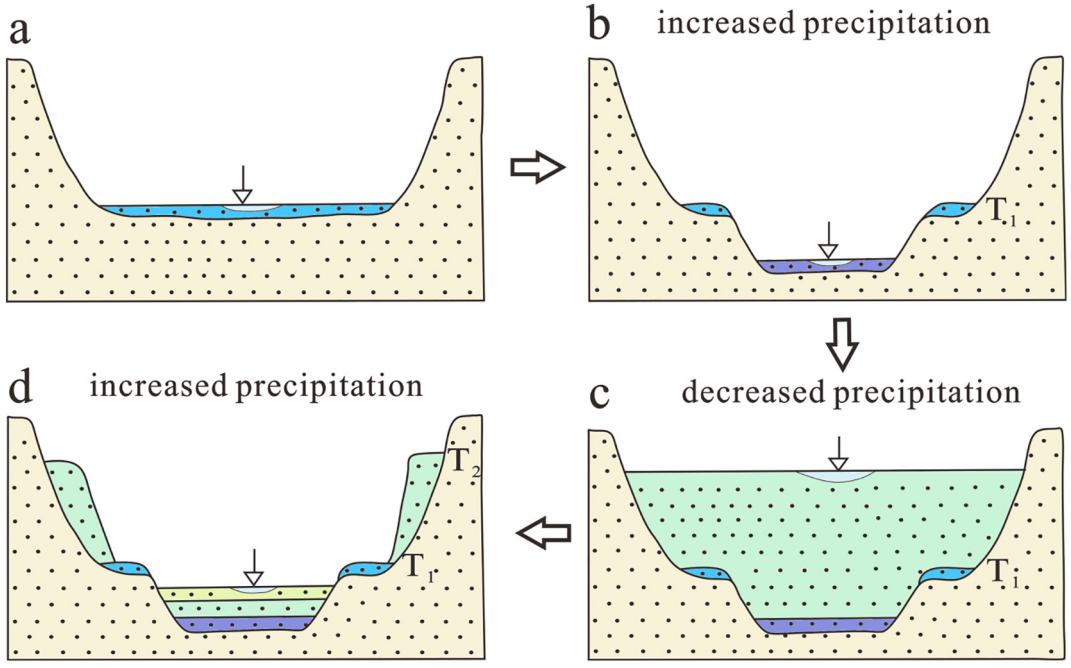

Fig. 9. Formation model of fluvial terraces along the Xilamulun River. Fluvial deposits at each time are marked with a different color. The aeolian deposits of the Hunshandake Sandy Land are light yellow in color.

glacial landform has been reported within the drainage basin of the Xilamulun River. Thus, it can be inferred that melt water has no influence on the long-term changes in the runoff. We believe that the main factor affecting the runoff of the Xilamulun River is precipitation. Modern observations reveal that the annual runoff has changed proportionally with the annual precipitation (Liu and Yang, 2000). Thus, a river will downcut due to the increased sediment discharge induced by increased precipitation.

Aeolian sand activity will interact with the fluvial processes of a river in a desert (Loope et al., 1995; Lepper and Scott, 2005). Many factors, including the sand source, vegetation coverage, wind strength and precipitation, can influence the amount of aeolian sand entering a channel (Schlesinger et al., 1990; Preusser et al., 2002; Cohen et al., 2010; Hall and Goble, 2015). The vegetation coverage is mainly controlled by precipitation (Loope et al., 1995). The summer monsoon and winter monsoon in this region vary inversely with regard to their phase (Jin et al., 2004; Xiao et al., 2008). A weakened summer monsoon leads to a reduction in the precipitation, which results in a diminished vegetation coverage, and a strengthened winter monsoon will enhance aeolian activity. As a result, the riverbed will aggrade and rise due to an increased aeolian sand input. Meanwhile, a strengthened summer monsoon will lead to an opposite scenario, i.e., the erosion and depression of the riverbed. For this reason, we infer that the height of the riverbed of the Xilamulun River could be used to indicate changes in precipitation, i.e., a higher riverbed height correlates with less precipitation.

If the formation model mentioned above is valid, then we can deduce the variation in regional precipitation. That is, there was relatively less precipitation at 36.2 ka, 27.5 ka, 23.6 ka, 18 ka, 11.1 ka, 8.4 ka, and 2.7 ka and relatively more precipitation at 25.8 ka, 21.9 ka, 11.3 ka, 8.6 ka, 7.9 ka, and 1.1 ka. Some lines of paleoclimate evidence indeed support this interpretation. Strengthened aeolian activities at 8.21 ka and 2.73 ka in the Hunshandake Sandy Land have been reported (Zhou et al., 2008), and their times coincide with reduced precipitation at 8.4 ka and 2.7 ka, respectively. Two arid intervals at 21.4 ka and 25.1 ka have been detected in coastal dunes in South China (Han et al., 2015) that may be approximately correlated with reduced precipitation at 23.6 ka. The high water level at 11.5 ka in Dali Lake in the Hunshandake Sandy Land (Xiao et al., 2008) may be another indicator of increased precipitation at 11.3 ka. A pollen-based quantitative precipitation reconstruction from Gonghai Lake in North China reveals a maximum monsoon intensity since 7.8 ka (Chen et al., 2015), which agrees well with an increase in the precipitation at 7.9 ka. Increased precipitation during the Medieval Warm Period was also recorded in historical documents (Zhang and Lu, 2007). Other evidence also points to an increase in precipitation at approximately 1.1 ka, including the formation of paleosols from 1.3 ka to 0.7 ka in the Hunshandake Sandy Land (Jin et al., 2004) and relatively strong chemical weathering from 1.2 ka to 0.9 ka in Daihai Lake (Jin et al., 2002).

6. Conclusions

The upper reach of Xilamulun River within the Hunshandake Sandy Land developed climatic terraces. The terrace ages do not increase with the terrace height as the result of a dynamic equilibrium between the sediment discharge and aeolian sand input. The higher-elevation terraces were deposited during a period of decreased precipitation when the sediment discharge was low and the aeolian sand input was high; the lower-elevation terraces were deposited under the opposite conditions. It is therefore clear that cyclic changes in the climate are capable of driving terrace formation even in the absence of background uplift.

Acknowledgments

We thank Gang Chen for his guidance with the technique of ArcGIS analysis and Xiaokang Yuan, Nairui Wang, and Bin Zhang for their assistance during the fieldwork. Jef Vandenberghe made some suggestions for revising the manuscript. This research was jointly supported by the National Natural Science Foundation of China (No. 41690111, 41671191 and 41571188) and the China Geological Survey (No. 21201102000150010-07).

References

Blum, M.D., 2013. Glacial–interglacial scale fluvial responses. In: Elias, S.A. (Ed.), Encyclopedia of Quaternary Science, Second Edition, pp. 112–125 (ISBN: 978-0-444-53642-6).
Bridgland, D., Westaway, R., 2008. Climatically controlled river terrace staircases: a worldwide Quaternary phenomenon. Geomorphology 98, 285–315.

Bullard, J.E., McTainsh, G.H., 2003. Aeolian-fluvial interactions in dryland environments: examples, concepts and Australia case study. Prog. Phys. Geogr. 27, 471–501.
Chen, F., Xu, Q., Chen, J., 2015. East Asian summer monsoon precipitation variability since the last deglaciation. Sci. Rep. 5, 11186.
Clark, G.M., Woods, P.F., 2000. Transport of Suspended and Bedload Sediment at Eight Stations in the Coeur d'Alene River Basin, Idaho. US Department of the Interior, US Geological Survey, California.
Cohen, T.J., Nanson, G.C., Larsen, J.R., Jones, B.G., Price, D.M., Coleman, M., Pietsch, T., 2010. Late Quaternary aeolian and fluvial interactions on the Cooper Creek Fan and the association between linear and source-bordering dunes, Strzelecki Desert, Australia. Quat. Sci. Rev. 29, 455–471.
DiBiase, R.A., Whipple, K.X., 2011. The influence of erosion thresholds and runoff variability on the relationships among topography, climate, and erosion rate. J. Geophys. Res. Earth Surf. 116, F04036.
Doğan, U., 2011. Climate-controlled river terrace formation in the Kızılırmak Valley, Cappadocia section, Turkey: inferred from Ar–Ar dating of Quaternary basalts and terraces stratigraphy. Geomorphology 126, 66–81.
Faye, R.E., Carey, W.P., Stamer, J.K., Kleckner, R.L., 1978. Erosion, Sediment Discharge, and Channel Morphology in the Upper Chattahoochee River Basin, Georgia. US Department of the Interior, US Geological Survey.
Goldsmith, Y., Broecker, W.S., Xu, H., Polissar, P.J., deMenocal, P.B., Porat, N., Lan, J., Cheng, P., Zhou, W., An, Z., 2017. Northward extent of East Asian monsoon covaries with intensity on orbital and millennial timescales. Proc. Natl. Acad. Sci. U. S. A. 114, 1817–1821.
Gulick, V.C., 2001. Origin of the valley networks on Mars: a hydrological perspective. Geomorphology 37, 241–268.
Hall, S.A., Goble, R.J., 2015. OSL age and stratigraphy of the Strauss sand sheet in New Mexico, USA. Geomorphology 241, 42–54.
Han, G., Zhang, G., Dong, Y., 2007. A model for the active origin and development of source-bordering dunefields on a semiarid fluvial plain: a case study from the Xiliaohe plain, Northeast China. Geomorphology 86, 512–524.
Han, Z., Li, X., Yi, S., 2015. Extreme monsoon aridity episodes recorded in South China during Heinrich events. Palaeogeogr. Palaeoclimatol. Palaeoecol. 440, 467–474.
Irwin, R.P., Craddock, R.A., Howard, A.D., 2005. Interior channels in Martian valley networks: discharge and runoff production. Geology 33, 489–492.
Jin, Z., Shen, J., Wang, S., 2002. The medieval warm period in the Daihai area. J. Lake Sci. 14, 209–216 (in Chinese).
Jin, H., Su, Z., Sun, Z., 2003. Characters of chemical elements in strata of middle and late Holocene in Hunshandake desert and the indicating climatic changes. J. Desert Res. 23, 366–371 (in Chinese).
Jin, H., Su, Z., Sun, L., Sun, Z., Zhang, H., Jin, L., 2004. Holocene climatic change in Hunshandake Desert. Chin. Sci. Bull. 49, 1730–1735.
Lepper, K., Scott, G.F., 2005. Late Holocene aeolian activity in the Cimarron River valley of west–central Oklahoma. Geomorphology 70, 42–52.
Liu, S., Yang, S., 2000. The regional variation sediment of transport in Asia. Mar. Sci. Bull. 19, 32–40 (in Chinese).
Liu, S., Deng, C., Xiao, J., 2016. High-resolution enviromagnetic records of the last deglaciation from Dali Lake, Inner Mongolia. Palaeogeogr. Palaeoclimatol. Palaeoecol. 454, 1–11.
Loope, D.B., Swinehart, J.B., Mason, J.P., 1995. Dune-dammed paleovalleys of the Nebraska Sand Hills: intrinsic versus climatic controls on the accumulation of lake and marsh sediments. Geol. Soc. Am. Bull. 107, 396–406.
Lu, H., Huissteden, K.V., An, Z., 1999. East Asia winter monsoon variations on a millennial time-scale before the last glacial–interglacial cycle. J. Quat. Sci. 14, 101–110.
Lu, H., Miao, X., Zhou, Y., 2005. Late Quaternary aeolian activity in the Mu Us and Otindag dune fields (north China) and lagged response to insolation forcing. Geophys. Res. Lett. 32, L21716.
Maddy, D., Bridgland, D.R., Green, C.P., 2000. Crustal uplift in southern England: evidence from the river terrace records. Geomorphology 33, 167–181.
Mason, J.A., Swinehart, J.B., Goble, R.J., 2004. Late-Holocene dune activity linked to hydrological drought, Nebraska Sand Hills, USA. The Holocene 14, 209–217.
Merritts, D.J., 2007. Fluvial environments: terrace sequences. In: Elias, S.A. (Ed.), Encyclopedia of Quaternary Science, pp. 694–702 (ISBN: 978-0-444-52747-9).
Murray, A.S., Wintle, A.G., 2000. Luminescence dating of quartz using an improved single-aliquot regenerative-dose protocol. Radiat. Meas. 32, 57–73.
Penkman, K.E.H., Preece, R.C., Bridgland, D.R., 2011. A chronological framework for the British Quaternary based on Bithynia opercula. Nature 476, 446–449.
Preusser, F., Radies, D., Matter, A., 2002. A 160,000-year record of dune development and atmospheric circulation in southern Arabia. Science 296, 2018–2020.
Schlesinger, W.H., Reynolds, J.F., Cunningham, G.L., 1990. Biological feedbacks in global desertification. Science 247, 1043–1048.
Srivastava, P., Brook, G.A., Marais, E., 2005. Depositional environment and luminescence chronology of the Hoarusib River Clay Castles sediments, northern Namib Desert, Namibia. Catena 59, 187–204.
Thomas, D.S.G., Stokes, S., Shaw, P.A., 1997. Holocene aeolian activity in the southwestern Kalahari Desert, southern Africa: significance and relationships to late-Pleistocene dune-building events. The Holocene 7, 273–281.
Tooth, S., 1999. Floodouts in central Australia. In: Miller, A.J., Gupta, A. (Eds.), Varieties of Fluvial Form, pp. 219–247 (ISBN:0471973513.
Törnqvist, T.E., 2007. Responses to rapid environmental change. In: Elias, S.A. (Ed.), Encyclopedia of Quaternary Science, pp. 686–694 (ISBN: 978-0-444-52747-9).
Tsakalos, E., Christodoulakis, J., Charalambous, L., 2015. The dose rate calculator (DRc)—a Java application for dose rate and age determination based on luminescence and ESR dating. Archaeometry 58, 347–352.
Wintle, A.G., Murray, A.S., 2006. A review of quartz optically stimulated luminescence characteristics and their relevance in single-aliquot regeneration dating protocols. Radiat. Meas. 41, 369–391.
Xiao, J., Si, B., Zhai, D., 2008. Hydrology of Dali lake in central-eastern Inner Mongolia and Holocene East Asian monsoon variability. J. Paleolimnol. 40, 519–528.
Xiao, J., Chang, Z., Si, B., 2009. Partitioning of the grain-size components of Dali Lake core sediments: evidence for lake-level changes during the Holocene. J. Paleolimnol. 42, 249–260.
Yang, X., Scuderi, L.A., Wang, X., 2015. Groundwater sapping as the cause of irreversible desertification of Hunshandake Sandy Lands, Inner Mongolia, northern China. Proc. Natl. Acad. Sci. U. S. A. 112, 702–706.
Zhang, D., Lu, L., 2007. Anti-correlation of summer/winter monsoons? Nature 445, 74–77.
Zhang, J., Yuan, B., Zhou, L., 2008. Luminescence chronology of "Old Red Sand" in Jinjiang and its implications for optical dating of sediments in South China. Chin. Sci. Bull. 53, 591–601.
Zhou, Y., Lu, H., Zhang, J., 2005. Active and inactive phases of sand dune in Mu Us and Otindag Sandlands during Late Quaternary suggested by OSL dating. J. Desert Res. 25, 342–350 (in Chinese).
Zhou, Y., Lu, H., Mason, J.A., Miao, X., Swinehart, J., Goble, R., 2008. Optically stimulated luminescence dating of Aeolian sand in the Otindag dune field and Holocene climate change. Sci. China Ser. D Earth Sci. 51, 837–847.
Zhou, Y., Lu, H., Zhang, X., 2013. Changes of the border of Otindag sand field (northern China) during the last glacial maximum and Holocene optimum. Quat. Sci. 33, 228–242 (in Chinese).